Atmospheric Environment 52 (2012) 67–81

Contents lists available at SciVerse ScienceDirect

Atmospheric Environment

journal homepage: www.elsevier.com/locate/atmosenv

Analysis of sub-micron parameters derived from multi-altitude and multi-spectral AOD measurements acquired during the 2009 PAM-ARCMIP airborne campaign

Auromeet Saha [a,*], Norman T. O'Neill [a,1], Robert S. Stone [b,c], Peter S. Liu [d], Andreas B. Herber [e]

[a] CARTEL, Université de Sherbrooke, Sherbrooke, Québec, Canada
[b] CIRES, University of Colorado, Boulder, USA
[c] NOAA Earth System Research Laboratory, Global Monitoring Division, Boulder, USA
[d] Science and Technology Branch, Environment Canada, Downsview, Canada
[e] Alfred Wegener Institute for Polar and Marine Research, Bremerhaven, Germany

ARTICLE INFO

Article history:
Received 22 April 2011
Received in revised form
25 October 2011
Accepted 15 November 2011

Keywords:
Airborne sunphotometry
Aerosol optical depth
Fine Mode effective radius
PAM-ARCMIP campaign
Ultra High Sensitivity Aerosol Spectrometer (UHSAS)

ABSTRACT

A series of Arctic sunphotometry flights were analyzed in terms of their multi-altitude, sub-micron (fine mode) information content. A spectral deconvolution algorithm (SDA) and a fine mode curvature algorithm (FMC) were applied to extract fine mode and coarse mode optical depth as well as the effective radius of the fine mode as a function of altitude. The fine mode optical depth was differentiated as a function of altitude to retrieve vertical profiles of fine mode extinction coefficient. These optical results were compared with volumetric altitude profiles of fine mode particle size distribution acquired by a UHSAS (Ultra High Sensitivity Aerosol Spectrometer).

The results showed that layer-averaged extinction cross sections derived from the ratio of fine mode optical depth to integrated UHSAS number density were significantly larger than extinction cross sections derived from the application of Mie theory to the UHSAS particle size distributions. Vertical profiles of extinction coefficients derived from altitude derivatives of the fine mode optical depth profiles showed some correlation with the UHSAS extinction coefficients. Profiles of the fine mode effective radius retrieved from the sunphotometry data were generally of similar magnitude to columnar averages of the UHSAS radii but no significant trend with altitude could be detected. An example was given of a high altitude smoke plume whose presence eliminated any hope of correlating the volumetric sampling information with the sunphotometer profiles. This is simply a statement of the obvious; that the atmospheric state must be stable in order to make such comparisons.

1. Introduction

The altitude variation of the density and size of aerosol particles is a critical component in understanding the dynamics of local, regional and global scale aerosol events. Over the Arctic this variation is complex and extends to relatively high altitudes during the late winter/early spring phenomenon known as Arctic Haze (Saha et al., 2010; Hoffman et al., 2009; Treffeisen et al., 2006). Arctic lidars such as the MPLNET lidar at Barrow Alaska, the CRL (CANDAC Rayleigh-Mie-Raman Lidar) and the AHSRL (Arctic High Spectral Resolution Lidar) instruments at the PEARL observatory in Eureka, Nunavut, Canada (Nott et al., in press and Saha et al., 2010 respectively) and the KARL (Koldeway Aerosol Raman Lidar) instrument at Ny-Ålesund, Spitsbergen (Hoffman et al., 2009) play an important role in characterizing these complex altitude dynamics (notably the AHSRL at Eureka which has maintained 24/7 operation, with some maintenance gaps, since August of 2005).

The acquisition of aerosol profiles over the Arctic using the (A-train) CALIOP lidar has achieved an operational status even if the interpretation can be hampered by the relatively lower signal to background noise characteristics of this system (i.e. compared to ground lidars). Significant high-Arctic aerosol events observed in CALIOP profiles are regularly reported in the literature. Airborne lidar measurements are necessarily intermittent (campaign dependent) in the Arctic but present target flexibility and instrumental resolution advantages (temporal, spatial and radiometric) that combine and complement the best features of ground-based and satellite lidars.

* Corresponding author. Tel.: +1 819 821 8000x61904; fax: +1 819 821 7944.
E-mail addresses: Auromeet.Saha@usherbrooke.ca, auromeet@gmail.com (A. Saha).
[1] On sabbatical leave during 2010/2011 at Dalhousie University, Halifax, Nova Scotia, Canada.

1352-2310/$ – see front matter © 2011 Elsevier Ltd. All rights reserved.
doi:10.1016/j.atmosenv.2011.11.037

While the temporal and vertical resolution of ground-based, airborne or satellite-based lidars are unmatched by any existing remote sensing device; aerosol retrievals associated with spectral curvature (notably retrievals related to aerosol size) are a significant challenge. This is due to the technical complexity of a multiple wavelength measurement and the weak inelastic returns of any Raman channels and attendant degraded signal-to-noise ratio and profile resolutions (G.J. Nott, personal communication).

1.1. Airborne sunphotometry

Airborne sunphotometry employs ground-based techniques adapted to the special requirements (notably solar tracking) of an aircraft environment. Relatively frequent measurements can be made during ascending or descending profiles to achieve vertically stratified aerosol optical depth (AOD) measurements which are sensitive to the aerosol vertical structure and which can be converted to extinction coefficient profiles. The derived profiles of extinction coefficient are analogous to lidar backscatter coefficient profiles except that they are fundamentally 2nd order in nature (the retrieval of an extinction coefficient from optical depth data is a somewhat unstable process) while being more optically tractable inasmuch as they are decoupled from the backscattering phase function (the intrinsic shortcoming of lidar profiles, inasmuch as phase-function-dependent lidar ratios are required as apriori input to convert backscatter coefficient profiles to extinction coefficient profiles). Of particular interest is the fact that the AOD measurements are made at a number of wavelengths in the visible and near-IR spectral region (and even the short-wave IR region; Shinozuka et al., 2011). These multi-band extinction measurements and the relatively good optical coherency of their inter-band signals are suited (i) to the extraction of simple but robust indicators of the columnar concentration of fine mode (sub-micron) particles (ii) to the retrieval of indicators of fine mode particle size (a similar statement applies to the retrieval of coarse mode optical depth and specifically to coarse mode particle size if the sunphotometry includes a short-wave IR channel, but this was not the case for the data we employed in this paper). It is the analysis and validation of points (i) and (ii) that we wish to pursue in this paper.

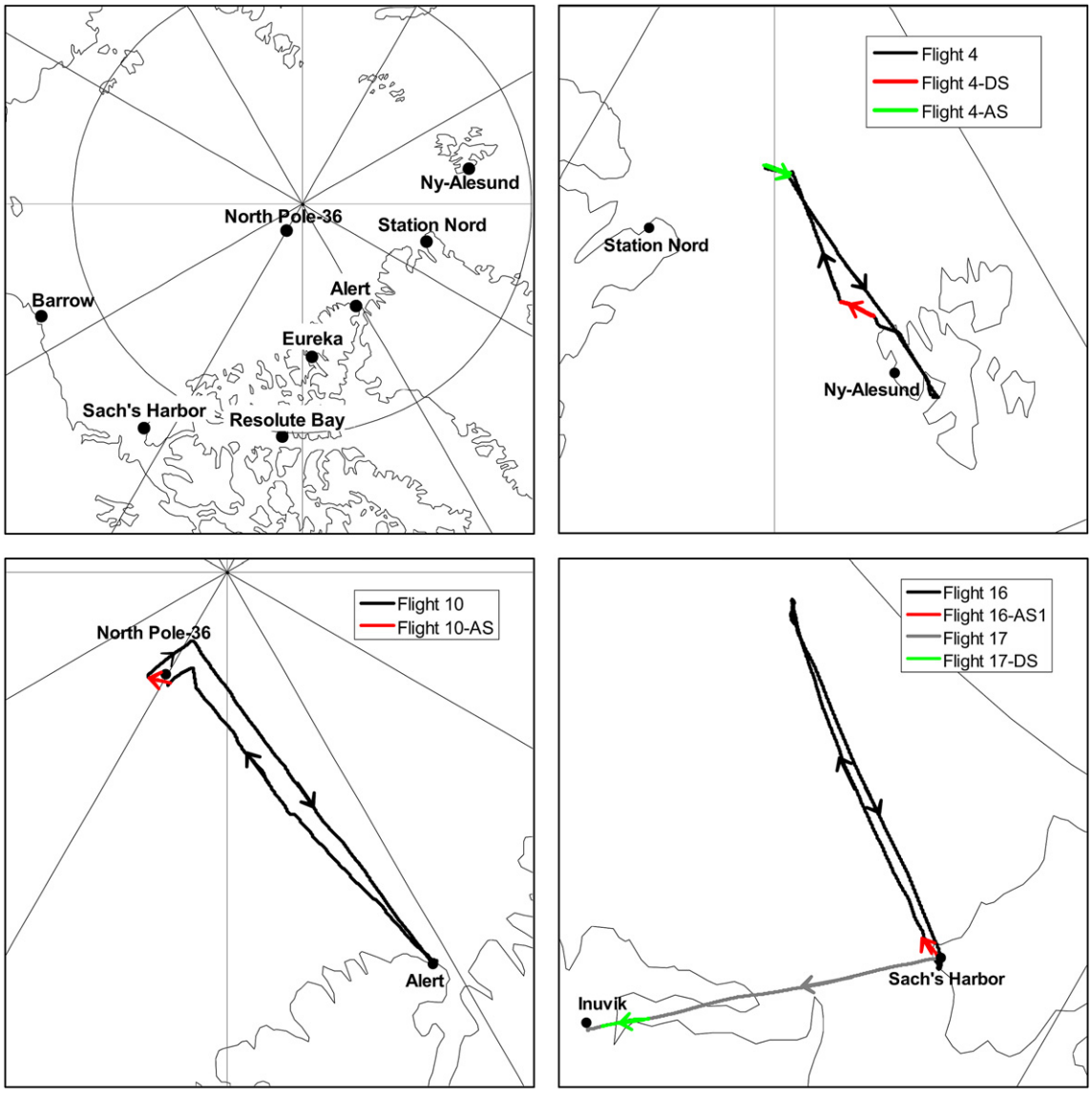

Fig. 1. General map of the stations employed during the PAM-ARCMIP campaign and sub-maps showing the flight lines whose data was used in this study.

Table 1
Flight line details. We have allowed ourselves a bit of symbolic license with respect to $\tau_f(0, \infty)$; the airborne vertical profiles that we dealt with had a minimum altitude which varied from a ~ hundred meters to greater than a km; rather than speak of z_{min} and complicate the nomenclature with z_{min} in addition to z_{max} we let "0" refer to the minimum altitude.

Date in 2009/ Start & End Time (UT)	Flight Number	Ascending (AS) or Descending (DS) Profile	Profile Start and End points/Nearest Station	Altitude Range (km)	$\tau_f(0, \infty)$	Remarks[a]
April 03 11:59–12:18	4	DS	Ny-Ålesund (NYA)	0.1–3.1	0.14	Profile dominated by coarse mode (probably thin clouds).
April 03 14:14–14:27	4	AS	Ny-Ålesund (NYA)	0.1–3.9	0.17	Boundary layer event (and a good example of low spectral noise).
April 10 18:14–18:21	10	AS	Alert (ALT) to North Pole-36 (NP-36)	0.3–2.0	0.10	Low turbidity event (in contrast to relatively high black carbon concentration).
April 16 20:14–20:21	16	AS-1	Sach's Harbor (SCH)	0.4–2.4	0.20	Strong AOD event below 1 km.
April 17 19:20–19:32	17	DS	Sach's Harbor (SCH) to Inuvik	1.2–3.0	0.08	AOD increased with increase in altitude. Profile influenced by smoke from southeastern Russia.

[a] as a starting point for inclusion in this table, all profiles where characterized by a relatively strong τ_f(lowest altitude value of $\tau_f(0, \infty) > 0.15$). The exceptions to this rule are the illustrative examples of the low turbidity (North Pole) case and the τ_c event of Flight 4-DS.

An airborne sunphotometry campaign was carried out during the April, 2009 PAM-ARCMIP (Pan-Arctic Measurements and Arctic Regional Climate Model Inter-comparison Project) circumpolar campaign using the Polar-5 research aircraft of the Alfred Wegener Institute (Stone et al., 2010). Numerous sunphotometer profiles for descending and ascending flight lines were acquired across the European and North American high-Arctic. Conditions varied from relatively clear to relatively turbid, the latter conditions being generally associated with the presence of significant Arctic Haze structure (ibid). Synchronous volumetric (submicron) particle size distributions were acquired using the UHSAS (Ultra High Sensitivity Aerosol Spectrometer). The Airborne Mobile Aerosol Lidar (AMALi) was also part of the Polar-5 instrument package (Lampert et al., in review); while this device was useful in helping us to confirm the behavior of sunphotometer AOD profiles, it has no capabilities for retrieving size information of fine mode particles. We accordingly opted to focus our comparisons on the UHSAS instrument. This communication is devoted to the interpretation of the multi-altitude sunphotometer retrievals and their comparison with UHSAS particle size distributions.

2. Methodology

2.1. PAM-ARCMIP campaign

The circumpolar campaign lasted from April 3 to April 25, 2009 and consisted of numerous flight lines carried out from high-Arctic stations between Ny-Ålesund (Spitsbergen) in the east to Barrow, Alaska in the west. The complete set of flight lines along with an overview of all instrumentation on the aircraft are described in Stone et al. (2010). In this paper we focused on descending or ascending profiles with continuously acquired sunphotometer and UHSAS measurements.

2.2. Instrumentation

A pair of temperature controlled, four-channel sunphotometers with a common solar tracker were employed to acquire airborne vertical profiles of AOD spectra. Wavelength subsets at 500, 610, and 778 nm and 412, 675, 862 nm respectively were combined to produce six channel AOD spectra (less accurate 367 nm and 1050 nm channels were eliminated from each four-channel set to ensure a better calibration accuracy for the combined set). These AOD spectra were ingested into our spectral processing algorithms (the SDA/FMC algorithms described below). Details on the calibration of the airborne sunphotometers, cloud screening and optical depth processing are given in Stone et al. (2010). For our purposes we note that the separate 3-channel sets were characterized by small estimated AOD errors of ~0.005.

Ambient aerosol was sampled via a forward facing diffuser type inlet. The aerosol sample in the inlet line was distributed to the various aerosol instruments on board the Polar 5. The aerosol instruments on the Polar 5 included a TSI Model 7610 Condensation Nucleus (CN) counter to measure particle (>14 nm) concentration, a Droplet Measurement Technologies (DMT) Ultra High Sensitivity Aerosol Spectrometer (UHSAS) to measure aerosol size distribution in the size range (radius) of 30–500 nm, and a DMT Single Particle Soot Photometer (SP-2) to measure black carbon concentration (Stone et al., 2010). For the purposes of this paper we employed the UHSAS in order to characterize the properties of the fine mode particle size distribution.

Dropsondes and downward looking AMALi profiles were collected from the Polar 5 aircraft on some of the flights while ground-based radiosonde profiles at certain stations were available at the beginning or terminal points of a few flights. The dropsondes yielded numerous meteorogical soundings along the Polar 5 track using transponder packages deployed from the aircraft (Dethloff et al., 2009). The AMALi provided downward looking backscatter ratio profiles at 532 nm (Stachlewska et al., 2010; Lampert et al., in review).

2.3. Spectral deconvolution and fine mode curvature algorithms

In this paper we employed the Spectral Deconvolution Algorithm (SDA) and Fine Mode Curvature (FMC) algorithm discussed in O'Neill et al. (2003) and O'Neill et al. (2008a). The SDA transforms AOD spectra into fine and coarse mode optical depths and fine mode Angstrom exponent at a reference wavelength (τ_f, τ_c and α_f at, typically, 500 nm) while the FMC transforms the fine mode α_f and its spectral derivative (α_f') into an estimate of fine mode effective radius ($r_{\mathrm{eff},f}$). This latter retrieval has been subject to a limited amount of validation (Toledano et al., 2011; Atkinson

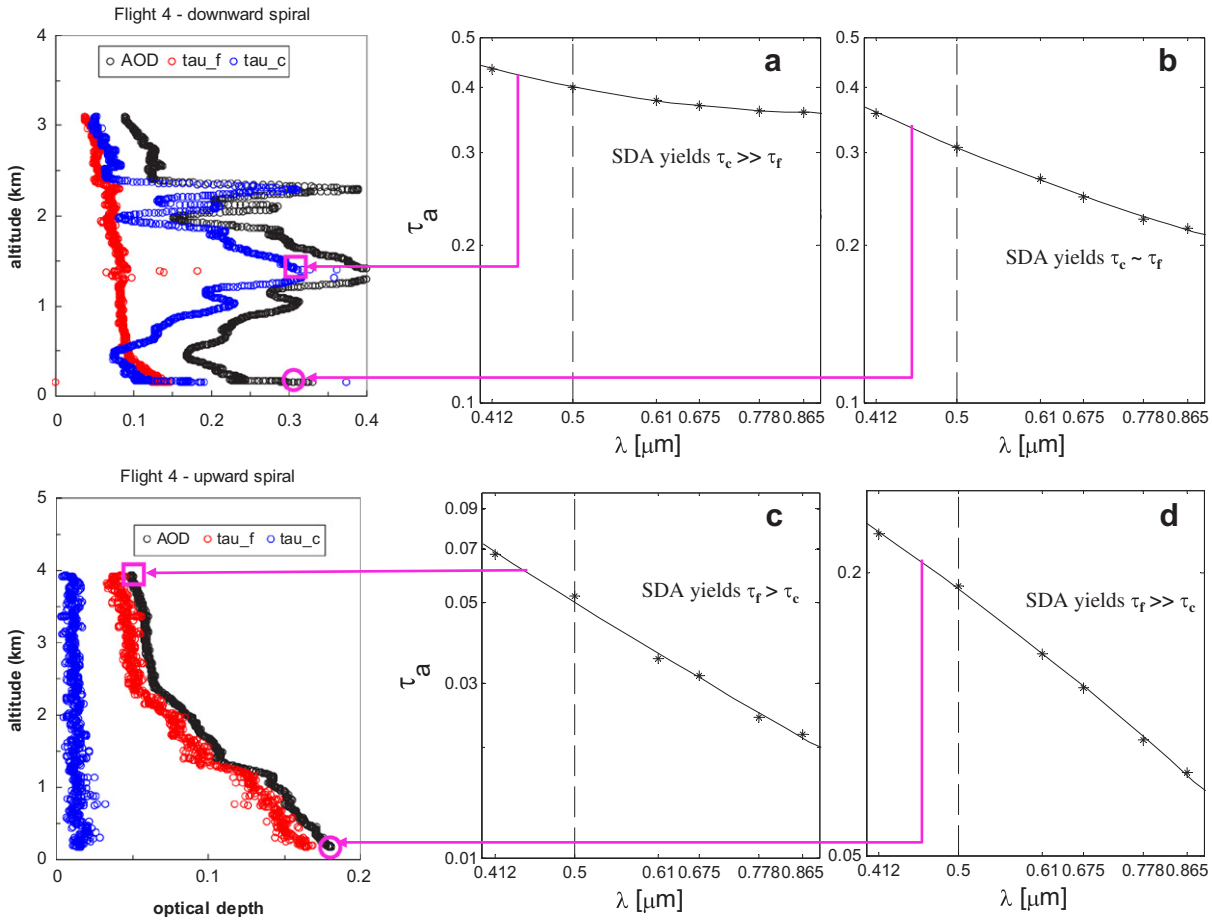

Fig. 2. Illustrative spectra and their effects on the retrieval in the case of stable spectral variations.

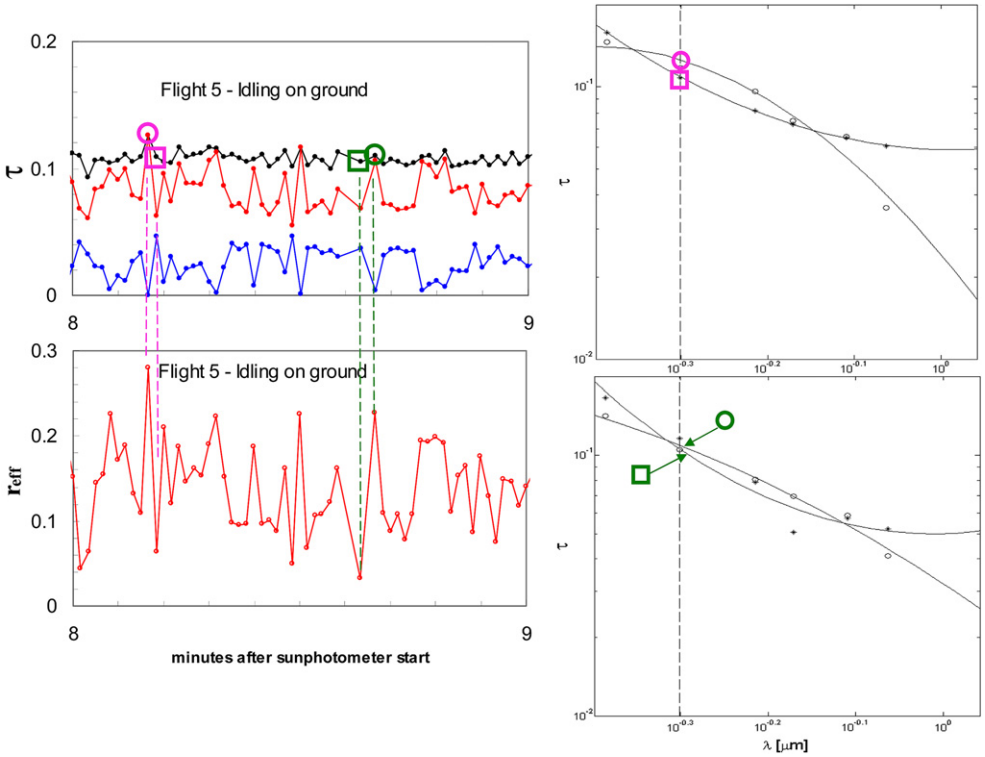

Fig. 3. Illustrative spectra and their effects on the retrieval in the case of noisy spectral variations. These were sunphotometer tests when the aircraft was idling on the tarmac prior to the commencement of Flight 5 (a flight line whose data was not employed in this study).

Table 2
Comparative statistics of the UHSAS and sunphotometry data.

Flight	$r_{N,f}\,(0, z_{max})$ [μm]	$\sigma_f\,(0, z_{max})$	$r_{eff,f}\,(0, z_{max})$ [μm]	$A_N\,(0, z_{max})$ [Mcm^{-2}]	$\tau_f\,(0, z_{max})$	$C_{ext,f,emp.}$ [ncm^2]	$C_{ext,f,Mie}$ [ncm^2]
4DS	0.067	1.66	0.125	101.05	0.100	0.98	0.241
4AS	0.075	1.63	0.134	57.2	0.127	2.21	0.330
10A	0.070	1.65	0.127	36.4	0.023	0.63	0.290
16AS1	0.077	1.74	0.136	38.4	0.118	3.07	0.534
17DS	0.066	1.60	0.117	42.23	0.223	5.28	0.175

et al., 2010; O'Neill et al., 2005); our objective here was to apply a spectral curvature analysis to the airborne AOD profiles acquired during the PAM-ARCMIP campaign in order to better understand what fine/coarse mode information could be retrieved as a function of altitude and if these retrievals were coherent with available validation data.

In order to retrieve $r_{eff,f}$ from the SDA/FMC algorithm one must estimate the real part of the refractive index (m_r of $m = m_r - m_i\,i$) for fine mode aerosols (O'Neill et al., 2008a). This value was taken as 1.48 while m_i was taken to be negligibly small (small, in terms of affecting $|m - 1|$). A survey of AERONET retrievals at 5 high-Arctic sites [Barrow (Alaska, USA), AEROCAN/AERONET sites at Resolute Bay and Eureka in Nunavut (Canada), Thule (Greenland, Denmark) and Hornsund (Spitsbergen, Norway)] yielded a mean and standard deviation of 1.48 ± 0.06 for April, 2009 ($N = 284$). The standard deviation of 0.06 is

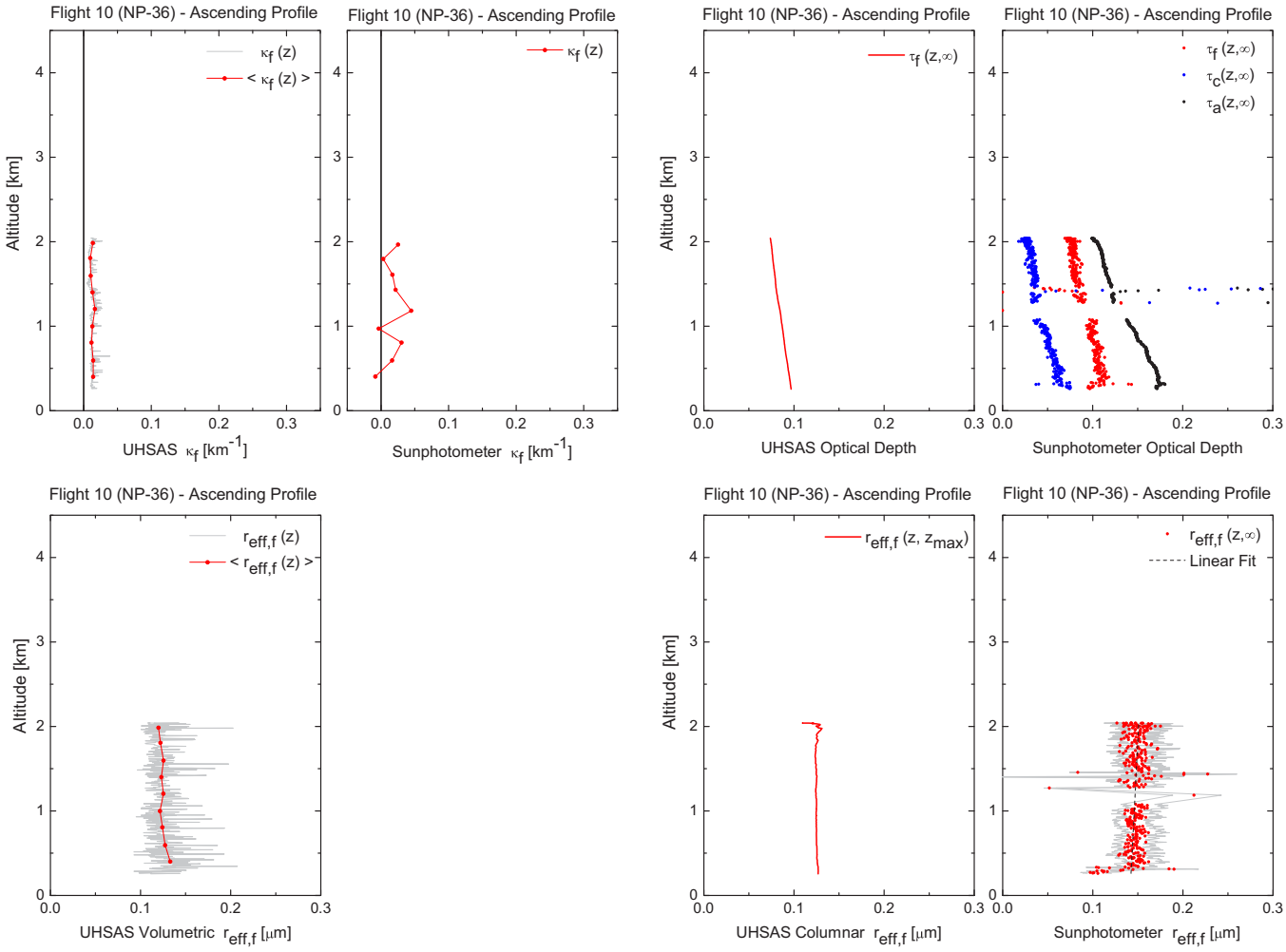

Fig. 4. Comparison of the UHSAS optical parameters derived from measured particle size distribution measurements (and the empirical extinction cross sections of Table 2) and the sunphotometry SDA/FMC retrievals for Flight 10 (low turbidity, North Pole case). The top row of graphs from left to right show (i) the fine mode extinction coefficient ($\kappa_f(z)$) derived for the UHSAS (both the original non filtered data and the same data averaged over altitude increments of 200 m), (ii) fine mode extinction coefficients ($\kappa_f(z)$) which result from altitude derivatives applied to the $\tau_f\,(z, \infty)$ sunphotometer profiles after these have been averaged over altitude increments of 200 m and filtered for excessive $\tau_c\,(z, \infty)$ excursions ($|d\tau_c\,(z, \infty)/dt| < 0.2$ per minute) (iii) the integration of $N_f(z)$ to obtain $A_N\,(z, z_{max})$ which is then transformed to a UHSAS estimate of $\tau_f\,(z, \infty)$ using equation (1b) and (iv) the optical depth profiles retrieved using the SDA/FMC algorithm applied directly to the sunphotometer spectra without altitude averaging or filtering. The boxes surround those pairs of graphs which can be directly compared. The bottom row of graphs from left to right show (i) the UHSAS estimate of $r_{eff,f}\,(z)$ (equation (2a)), (ii) a blank space for the excessively noisy estimates of $r_{eff,f}\,(z)$ from sunphotometry spectra of $\kappa_a\,(z)$ (iii) the UHSAS-derived columnar estimate of $r_{eff,f}\,(z, z_{max})$ as per equation (3) and (iv) $r_{eff,f}\,(z, \infty)$ estimates from the sunphotometry (the red curves show the estimates using the nominal value of m_r (1.48) while the gray curves show the uncertainty in the retrieval associated with uncertainty of 0.06 in m_r. (For interpretation of the references to color in this figure legend, the reader is referred to the web version of this article.)

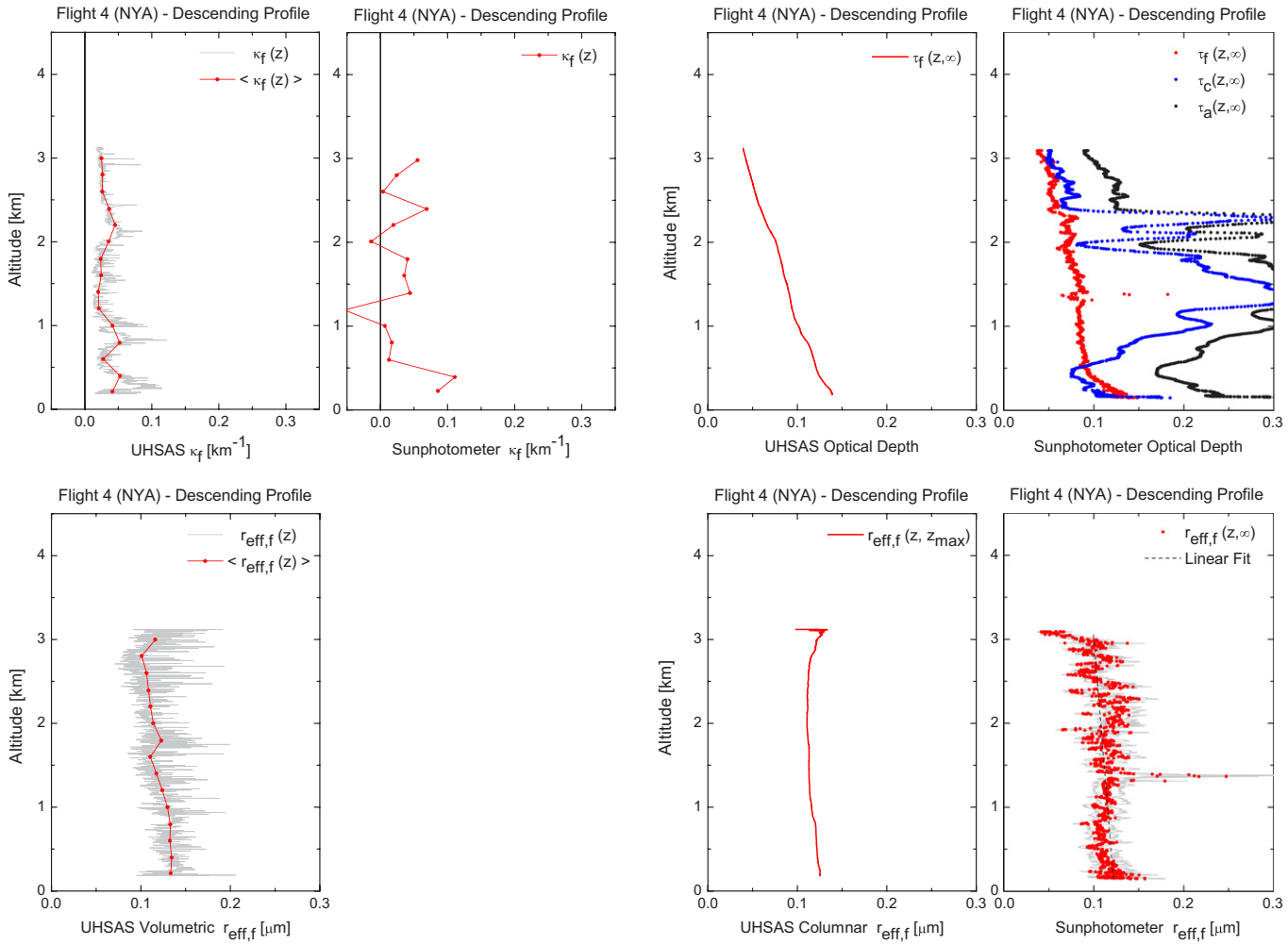

Fig. 5. Comparison of UHSAS and sunphotometer retrievals for the case of a strong coarse mode intrusion (near the beginning of Flight 4). Same description as for Fig. 4.

commensurate with the estimated retrieval error of 0.05 for 440 nm AODs smaller than 0.2[2] (Dubovik et al., 2000). A value of $m_r = 1.48$ is also close to the value of 1.50 determined for Arctic Haze aerosols by Tomasi et al. (2007).

2.4. Comparison of UHSAS and sunphotometry data

The reader is invited to consult the Appendix where we deal with the physical and mathematical details of comparing columnar (sunphotometer) and volumetric (UHSAS data). He or she should also refer to the acronym and symbol glossary (the usage of these succinct symbols saves a lot of inefficient repetition of text and actually clarifies the issues being discussed).

In order to compare the above-aircraft sunphotometry retrievals of $\tau_f\,(z,\,\infty)$ during an ascending or descending profile with the volumetric (fine mode) UHSAS number densities $[N_f\,(z)]$ one has to either take spatial derivatives of the former to extract extinction coefficient profiles (as described in the "Volumetric Relationships" section of the Appendix and as Stone et al. (2010) did for total aerosol extinction coefficients in their paper) or vertically integrate the latter to yield columnar abundances $[A_N\,(z,\,z_{max})$ as described in the "Columnar Relationships" section of the Appendix]. We chose to employ both approaches in order to illustrate the utility of both types of information (and sometimes to sidestep numerical problems).

2.5. Selection of flight lines

Fig. 1 shows a map of the PAM-ARCMIP flight lines that we chose to analyze and Table 1 gives specific details about each flight line (including the reasons for the choice). Flight lines were selected for analysis if τ_f values were fairly large (indicative of some type of fine mode event) and if the spectral noise was reasonably subdued. We were also influenced by the overview of the 2009 PAM-ARCMIP campaign given in Stone et al. (2010); these authors pointed out that the principle aerosol influence during the campaign was Arctic Haze (for which τ_f is typically dominant). Flight 17 was a large τ_f event but it was singled out specifically because the sunphotometry differed so much from the UHSAS results.

3. Results

3.1. Spectral curvature examples

Fig. 2 shows examples of SDA retrievals applied to vertical profiles of AOD spectra alongside explicit AOD spectra from which the retrievals were derived for sample altitudes [left and right of the figure respectively; in all our examples of retrievals we maintain a color assignment of black for the AOD from altitude z to ∞

[2] Which describes our April data set where the mean and standard deviation of AOD (440 nm) was 0.141 ± 0.053.

($\tau_a(z,\infty)$), red for $\tau_f(z,\infty)$ and blue for $\tau_c(z,\infty)$]. The specific altitude of the retrievals are circumscribed by magenta symbols that are linked to the associated AOD spectra on the right side of the figure. These cases vary from strongly fine mode [$\tau_f(z,\infty) >> \tau_c(z,\infty)$] to strongly coarse mode [$\tau_f(z,\infty) << \tau_c(z,\infty)$] and they show robust curvature; the points approximately align along classical spectral curvature curves which vary from convex downward to convex upward [for simplicity we omit the argument list "(z,∞)"]. This robust point curvature suggests that the retrievals are significant even for AODs which are rather small (for which nominal calibration errors of 0.005 represent a significant fraction).

3.2. Noisy spectra

Some of the sunphotometry data was subject to what one could describe as noisy spectral variation. Fig. 3 gives an example of a particularly egregious case. At the time, the plane was idling on the ground while test sunphotometer measurements were being made. While τ_a variations were relatively stable (black curve) large changes in τ_f and τ_c can be observed. The reason for these changes is evident in the associated AOD spectra; the obviously strong variations in spectral shape induce fundamental changes in the retrieval results of the SDA algorithm (not to mention the FMC whose results are not shown). Such anomalies inspired us to apply special altitude-binned filtering techniques in order to reduce the impact on the τ_f retrieval profiles when this problem was more evident (filtering which was clearly needed in some cases more than others).

3.3. Optical discrepancy between sunphotometry and UHSAS data

The extinction cross sections computed using a Mie code with inputs of geometric mean radius ($r_{N,f}$) and geometric standard deviation (σ_f) [obtained by computing means and standard deviation, in a logarithmic space, of the UHSAS particle size distributions] yielded extinction cross sections which were systematically and significantly lower than empirical extinction cross sections computed from the sunphotometer fine mode optical depths and the integrated UHSAS abundance [as per equation (1c) in the Appendix]. These computations, for all flight lines, are presented in Table 2 (the average ratio of $C_{f,\text{emp.}}$ to $C_{f,\text{Mie.}}$ was approximately 4.7). In spite of this anomalous result, we found that $C_{f,\text{emp.}}$ was rather strongly correlated with $C_{f,\text{Mie}}$ ($R^2 = 0.78$ excluding the non-homogeneous smoke event of Table 2); such a correlation,

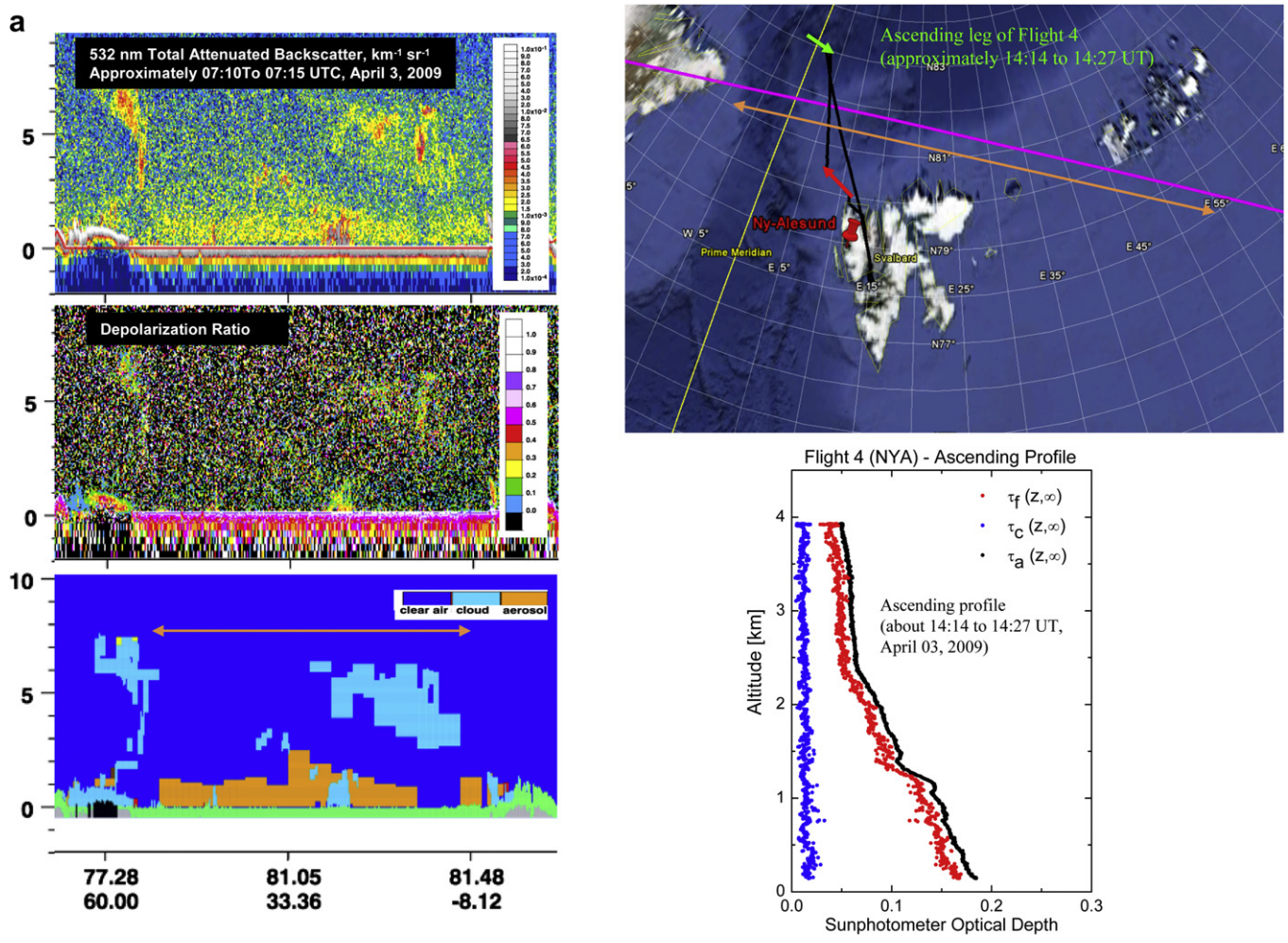

Fig. 6. (a) CALIOP support for the boundary layer event of April 3, 2009. The CALIOP images represent (top to bottom); attenuated backscatter coefficient ($km^{-1}\ sr^{-1}$) at 500 nm, depolarization ratio at 500 nm and feature classification. The map shows the CALIOP orbit line (and its direction) in magenta, the rough extent of the boundary layer aerosols indicated in orange on the CALIOP feature classification image and track of Flight 4 in black. The optical depth altitude profile (acquired near the coast of Spitsbergen and shown by a red arrow on the map) shows a boundary layer frontier (sharp change in slope) around 1 km in altitude). See Fig. 6b for retrieval details. (b) Comparison of UHSAS and sunphotometer retrievals for the case of the April 3, 2009 boundary layer event (near the end of Flight 4). Same description as for Fig. 4. (For interpretation of the references to color in this figure legend, the reader is referred to the web version of this article.)

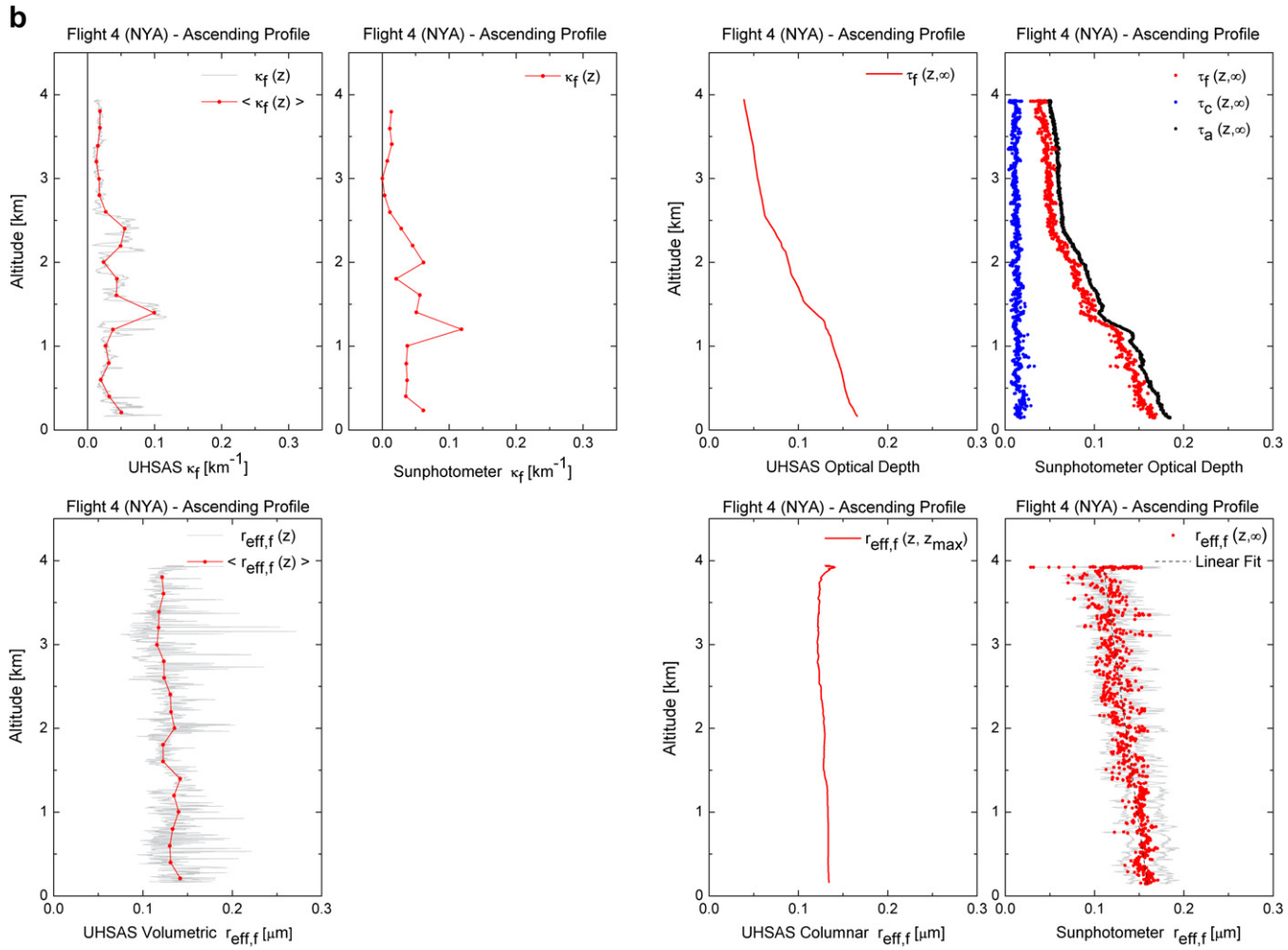

Fig. 6. (*continued*).

resulting from the comparison of totally independent data seems rather extraordinary, however it would be disingenuous on our part to make anything of this result since we don't understand the large amplitude differences in the cross sections.

The empirical extinction cross sections can be too large if $A_N(0, z_{max})$ is too small or if the difference $\tau_f(z, \infty) - \tau_f(z_{max}, \infty)$ is too large. We could not resolve this dilemma but nonetheless had to make a choice in terms of the mean extinction cross section employed to convert UHSAS values of $N_f(z)$ and $A_N(z, z_{max})$ to $\kappa_f(z)$ and $\tau_f(z, \infty)$ for purposes of comparison with the sunphotometry results. The empirical extinction cross section was selected because it was derived directly from the UHSAS and sunphotometry data set (it also necessarily gives much better comparison results in the analysis below).

3.4. Analysis of selected profiles

Figs. 4–8 represent five different types of aerosol cases that we chose to focus this work on; a low turbidity illustration taken near the North Pole, an example of an optical depth profile contaminated by thin homogeneous cloud, a boundary layer event northeast of Ny-Ålesund, a boundary layer event northeast of Sach's Harbor and a smoke event near Inuvik.

Fig. 4 shows a comparison of the UHSAS particle size distribution measurements and the sunphotometry SDA/FMC retrievals for the least turbid case (an ascending profile that was acquired near the North Pole and that was part of flight line 10 between Alert and the North Pole). This figure is interesting in its own right but also allows us to introduce the general organization of the vertical profile graphs of Figs. 4–8. The top row of the Fig. 4 graphs, from left to right, show (i) fine mode extinction coefficients $[\kappa_f(z)]$ computed from the total UHSAS fine mode concentration $[N_f(z)]$ using the empirical extinction cross sections of Table 2 (for both the original non filtered data and the same data averaged over altitude increments of 200 m), (ii) $\kappa_f(z)$ which result from the application of altitude derivatives to the $\tau_f(z, \infty)$ sunphotometer profiles [c.f. equation (4) in the Appendix] after these have been averaged over altitude increments of 200 m (the application of such derivatives to the unfiltered data was determined to be excessively noisy) (iii) the integration of UHSAS $\kappa_f(z)$ values to obtain UHSAS estimates of $\tau_f(z, \infty)$ using the Appendix equation (1b) and (iv) the fine, coarse and total aerosol optical depth profiles of $\tau_f(z, \infty)$, $\tau_c(z, \infty)$, and $\tau_a(z, \infty)$ (red, blue and black respectively) retrieved using the SDA/FMC algorithm applied directly to the sunphotometer spectra (without altitude averaging). One can then compare the shape of the $\kappa_f(z)$ altitude profiles for the first pair of graphs and the shape of the red $\tau_f(z, \infty)$ curves from the second pair of graphs. The bottom row of graphs from left to right show (i) the UHSAS estimate of $r_{eff,f}(z)$ [equation (2a) of the Appendix], (ii) a blank space for the estimates of $r_{eff,f}(z)$ from sunphotometry spectra of $\kappa_a(z)$ (iii) the UHSAS-derived columnar

estimate of $r_{eff,f}(z, z_{max})$ as per equation (3) of the Appendix and (iv) $r_{eff,f}(z, \infty)$ estimates from the sunphotometry (the red curves show the estimates using the nominal value of m_r while the gray curves show the uncertainty in the retrieval associated with uncertainty of 0.06 in m_r). The choice to not display estimates of $r_{eff,f}(z)$ from sunphotometry spectra of $\tau_a(z)$ was necessitated by the extremely unstable process of first taking spatial derivatives which tend to produce large variations in the $\kappa_a = -d\tau_a(z)/dz$ spectra and which in turn produce extremely large variations in derived quantities ($r_{eff,f}(z)$ in particular). The choice to display $r_{eff,f}(z, z_{max})$ for the UHSAS data rather than an estimate of $r_{eff,f}(z, \infty)$ [as per equation (3b) of the Appendix] was made in order to minimize the influence of the sunphotometer retrievals on this intensive parameter [in terms of equation (3b) this amounts to saying that we presumed $r_{eff,f}(z, z_{max}) \sim r_{eff,f}(z_{max}, \infty)$].

The $\kappa_f(z)$ profiles of Fig. 4 show relatively weak extinction ($\sim$0.01 km^{-1}) while the $\tau_f(z, \infty)$ profiles indicate no obvious boundary layer. The values of $\tau_f(0, \infty)$ are relatively small ($\sim$0.1) but still somewhat larger than typical background values (see, for example, O'Neill et al., 2008b); this may or may not have been associated with the presence of relatively elevated black carbon samples reported by Stone et al. (2010). The values of $r_{eff,f}(z, z_{max})$ in the case of the UHSAS and $r_{eff,f}(z, \infty)$ in the case of the sunphotometry are relatively small ($\sim$0.13 and 0.14 μm respectively) and are particularly noisy in the latter case.

Fig. 5 shows a case that was more or less dominated by coarse mode aerosols [blue $\tau_c(z, \infty)$ curve] that came into the sunphotometer FOV as the aircraft descended. We show this one example of variable τ_c domination to demonstrate the dynamic nature of the SDA algorithm [the large $\tau_c(z, \infty)$ variation in blue is probably due to thin homogeneous cloud and not some form of coarse mode aerosol; its low frequency signature is typical of optically thin, relatively homogeneous clouds] and to caution that the apparently good retrieval results for $r_{eff,f}(z, \infty)$ are, likely fortuitous because the second order curvature that is needed to generate size information is especially sensitive to coarse mode domination. We note that sunphotometer values of $\kappa_f(z)$ derived from the $\tau_f(z, \infty)$ profile are coherent to a certain extent with the UHSAS $\kappa_f(z)$ values (duplication of the larger value at the lowest altitudes and small if noisy values at higher altitudes). This represents a distinct improvement over an extinction coefficient that would have been derived from vertical derivatives of the (black-colored) $\tau_a(z, \infty)$ profile; this would have yielded wildly oscillating, negative to positive, extinction coefficients.

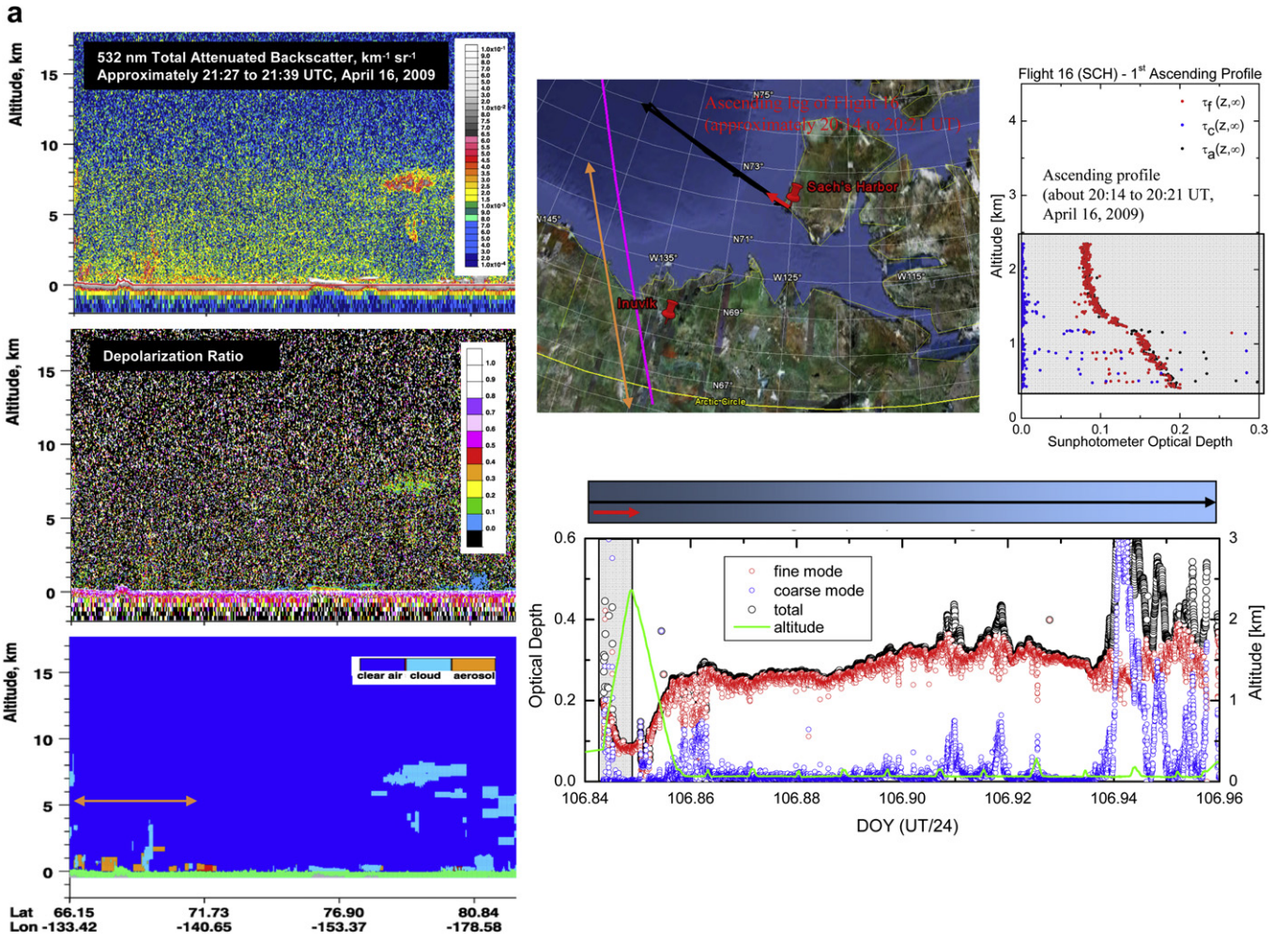

Fig. 7. (a) Support for the boundary layer event of April 16, 2009. The organization of the CALIOP images and the map is described in the caption of Fig. 6a. The graph in the bottom right hand corner shows the variation of optical depth as a function of time for the total flight line (shown in black on the map). The optical depth altitude profile (acquired near the beginning of Flight 16 and represented by a short red arrow on the map) shows a boundary layer frontier (sharp change in slope) around 1.2 km of altitude). See Fig. 7b for retrieval details. The green curve shows the aircraft altitude along the flight line. (b) Comparison of UHSAS and sunphotometer retrievals for the case of the April 16, 2009 boundary layer event (near the beginning of Flight 16). Same description as for Fig. 4. (For interpretation of the references to color in this figure legend, the reader is referred to the web version of this article.)

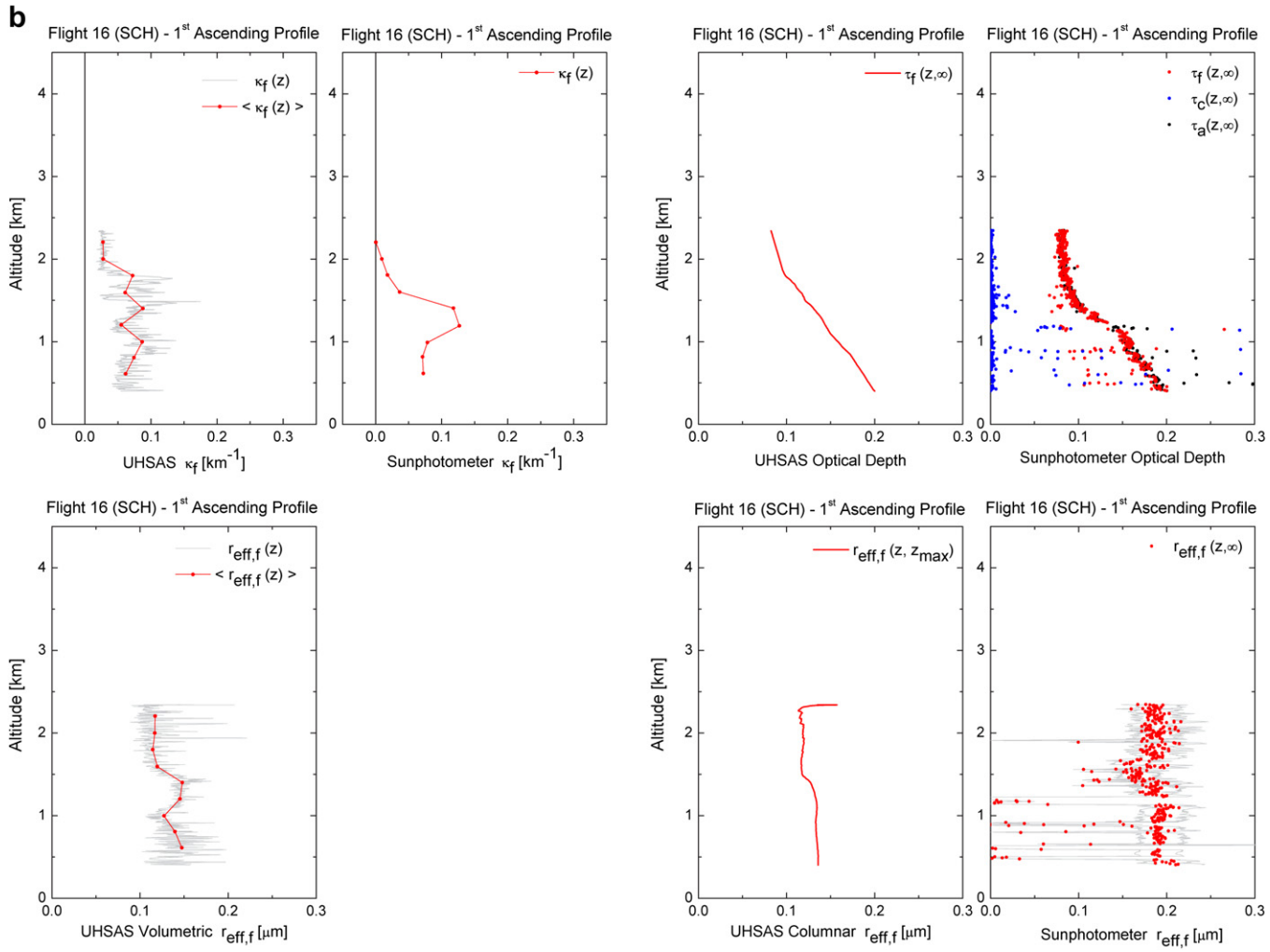

Fig. 7. (*continued*).

Fig. 6a shows the case of a substantial boundary layer event which the aircraft flew over during Flight 4. This case study was focused on an ascending profile that was acquired near the end of the Flight 4 (the flight line and a red arrow indicating the length and direction of the ascending profile are shown on the map). The figure also shows CALIOP profiles of attenuated backscatter coefficient (532 nm), depolarization ratio and the CALIOP feature classification profile acquired about 7 h before Flight 4 (the CALIOP orbit line and its direction is shown by a magenta line on the map). The CALIOP data show a fairly strong boundary layer event ($<\sim$1 km altitude) with relatively high values of attenuated backscatter coefficient and low depolarization ratio (typical of fine mode aerosols). The CALIOP feature classification algorithm labeled this perturbation as an aerosol event (orange colored class in the bottom CALIOP image); the approximate position of this aerosol class is shown in orange along the CALIOP orbit line on the map. Meteorological conditions for the day were under the influence of a stable high pressure system over the European and North American Arctic; it is accordingly likely that the conditions at the time of the CALIOP overpass were generally sustained until the passage of Flight 4. Fig. 6b shows what appears to be correlated $\kappa_f(z)$ profiles that are vertically offset by a few hundred meters (specifically for the two layers of fine mode aerosols which are evident in the UHSAS data at about 1.5 and 2.5 km). This is also evident in the $\tau_f(z, \infty)$ profiles where the subtle changes in slope which control the changes in $\kappa_f(z)$ are also offset by a few hundred meters. One can only hypothesize that inhomogeneities in the two layers of aerosols produce differing responses because the effective sampling volumes of the UHSAS and the sunphotometry are different. The $r_{\mathrm{eff},f}$ profiles are of similar magnitude (approximately 0.14 versus 0.16 μm for the UHSAS and sunphotometer respectively) with slopes that are slightly negative as a function of increasing altitude.

Fig. 7a shows what we believe to be a boundary layer event northeast of Sach's Harbor. The CALIOP profile data on the left of the figure was acquired only about an hour after the flight data (as in the case of Fig. 6a, the CALIOP orbit line, with orbit direction indicated, is shown in magenta on the map). In this case we focused on an ascending profile acquired very near the beginning of the flight (red arrow superimposed on the black colored, Flight line 16) and whose $\tau_f(z, \infty)$ profile is shown in the top right hand corner of the figure. In the bottom right corner of the image we have plotted the optical depth variation across the total flight line shown (the ascending profile is delimited by a semi-transparent gray rectangle on this graph as well as on the altitude versus optical depth graph). One can note that the proof of a boundary layer event in CALIOP data is somewhat marginal with only sporadic cells being classified as aerosol in the CALIOP feature classification image. However the

presence of an obvious boundary layer in the $\tau_f(z, \infty)$ profile and quite large $\tau_f(0, \infty)$ values along most of the flight line leads one to infer that there was a large scale boundary layer event within the general region of the flight line. Fig. 7b shows that an apparent boundary layer event is well captured by $\kappa_f(z)$ and $\tau_f(z, \infty)$ for the sunphotometry and captured at something better than a marginal level of significance by the UHSAS. The difference between $r_{\mathrm{eff},f}(z, z_{\max})$ from the UHSAS and $r_{\mathrm{eff},f}(z, \infty)$ from the sunphotometry is large; closer examination indicated that the UHSAS particle size distributions were complex (distinctly non log-normal) and that the use of standard mean indicators of particle size such as $r_{\mathrm{eff},f}$ was of questionable value.

In general the $\kappa_f(z)$ comparisons (UHSAS versus sunphotometry) show a marginally significant degree of correlation (with the exclusion of the Sach's Harbor to Inuvik case of Fig. 8a which is dealt with below). The $r_{\mathrm{eff},f}(z, z_{\max})$ values from the UHSAS computations and the $r_{\mathrm{eff},f}(z, \infty)$ values from the sunphotometry were, with the exception of Flight 16, fairly close in amplitude with some or no correlation as a function of altitude [within about 0.03 μm relative to the mean dashed line through the $r_{\mathrm{eff},f}(z, \infty)$ values]. The evidence that would suggest a decrease of $r_{\mathrm{eff},f}$ with altitude is marginal at best [Stone et al., 2010 suggested that there existed such a correlation in the UHSAS data but the decrease was less than 0.005 μm in UHSAS radius, something that we could hardly expect to see in the sunphotometry retrievals given, for example, the degree of noise seen in the $r_{\mathrm{eff},f}(z, \infty)$ profiles].

3.4.1. Special case of the Inuvik smoke plume

Fig. 8a shows an apparently anomalous situation where $\tau_f(z, \infty)$ decreased with descending altitude as the plane performed the descending profile just before landing in Inuvik. The UHSAS $A_{N,f}(z, z_{\max})$ values and their associated $\tau_f(z, z_{\max})$ values increased with decreasing altitude as one would expect in the absence of any variation of $\tau_f(z_{\max}, \infty)$. The problem was that $\tau_f(z_{\max}, \infty)$ varied in a substantial fashion due to a high altitude smoke plume coming into the FOV of the sunphotometer. It began slowly increasing from about a value of 0.06 half an hour out of Sach's Harbor (about 107.77 on Fig. 8b) and then rapidly increasing (at about 107.793) to a peak that occurred about 1 1/2 min before the plane began to descend. We have included the UHSAS fine mode number density measurements under the optical depth graph in Fig. 8b; we did this only to demonstrate

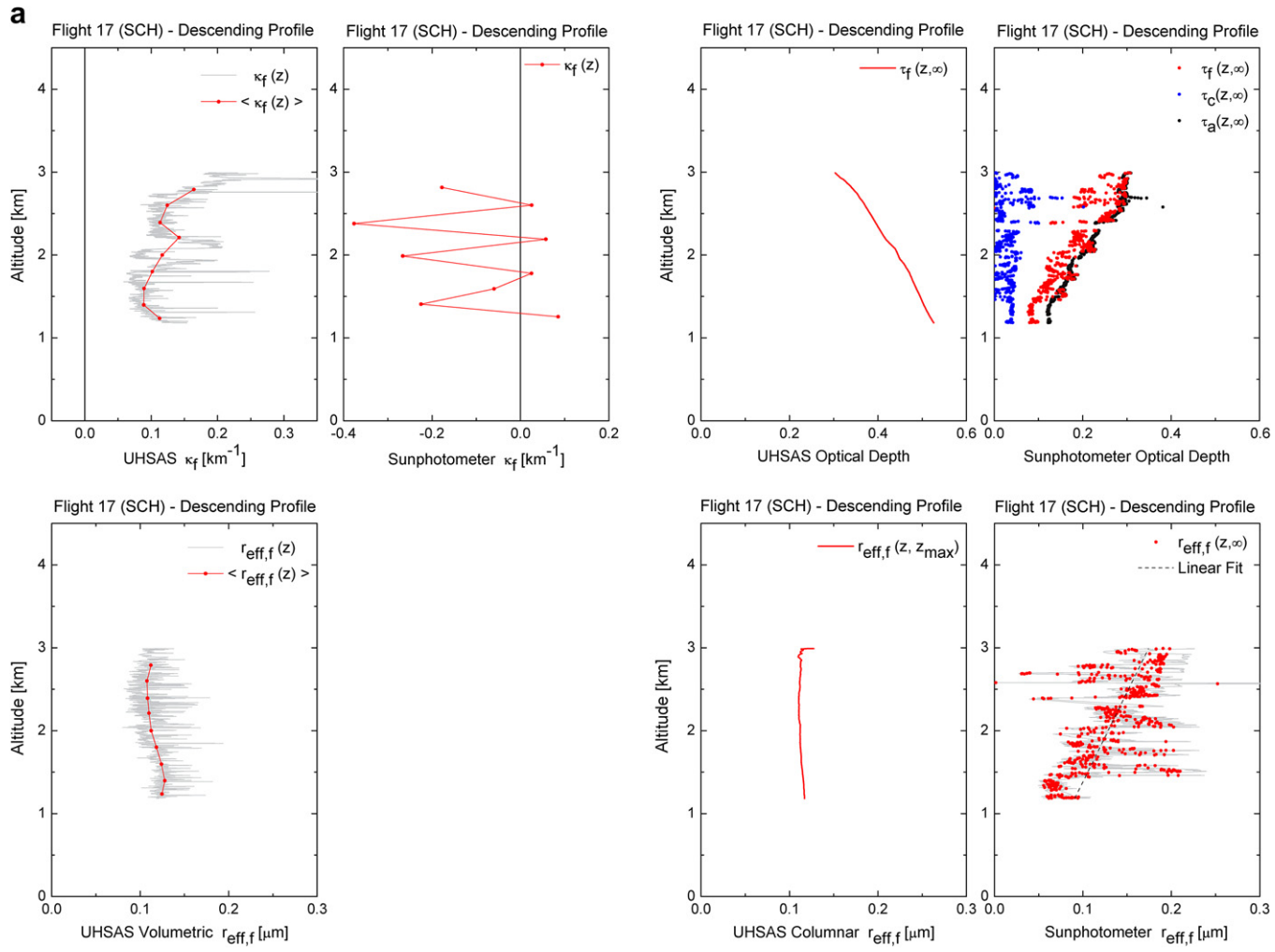

Fig. 8. (a) Comparison of UHSAS and sunphotometer retrievals for the case of the April 17, 2009 smoke event (Flight 17 near Inuvik). Same description as for Fig. 4. (b) The top graph shows the variation of $\tau_a(z, \infty)$, $\tau_f(z, \infty)$ and $\tau_c(z, \infty)$ as well as the aircraft altitude during Flight 17 from Sach's Harbor to Inuvik. The Bottom graph shows the variation of UHSAS fine mode number density ($N_f(z)$) during Flight 17. Green lines represent the aircraft altitude. (c) CALIOP image of the plume which affected the airborne sunphotometry on the April 17 flight from Sach's Harbor to Inuvik. In order for the southern end of the plume to arrive at Inuvik ~1930 UTC (the leading edge of the larger $\tau_f(z, \infty)$ disturbance seen in Fig. 8b between approximately 107.793 and 107.813) the backtrajectory indicates that the CALIOP plume position and timing is about right. (For interpretation of the references to color in this figure legend, the reader is referred to the web version of this article.)

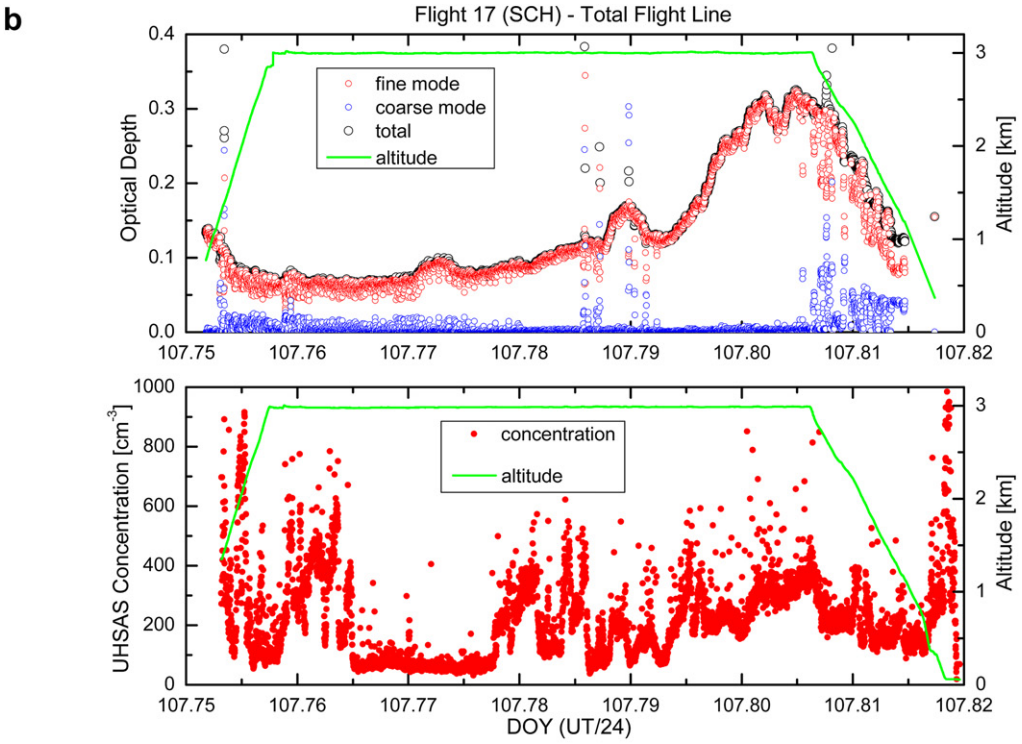

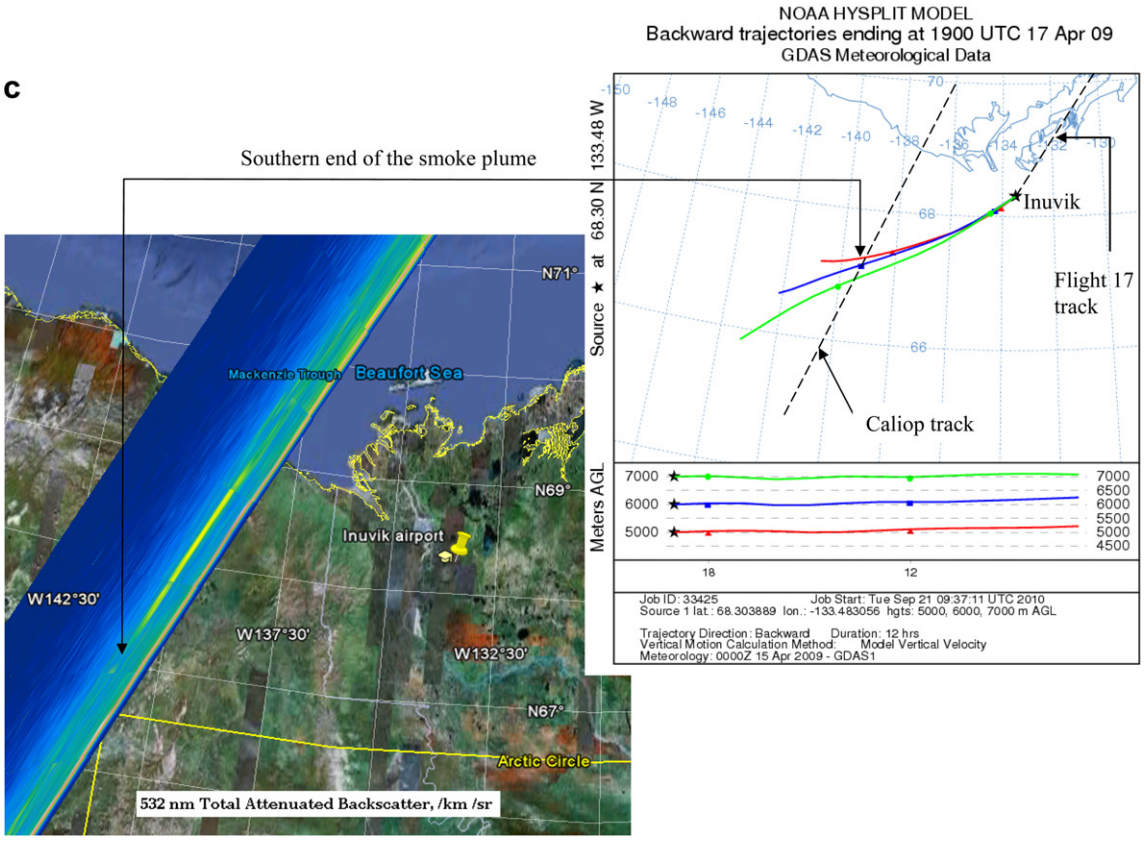

Fig. 8. (*continued*).

that in spite of the plane being about 3 km below the smoke plume there seemed to be some residual smoke which affected the UHSAS measurements.

Fig. 8c shows that this anomalous example was the result of a smoke plume at about 6 km altitude (well above the airplane) whose southern end passed over Inuvik at about 1930 UT (107.8125 in Fig. 8b). The plume was nicely captured by the CALIOP lidar and was associated with low values of depolarization ratio, a necessary but not sufficient condition for the presence of smoke. Backtrajectories from Inuvik, MODIS images of fire hotspots and source smoke and Fire Locating and Modeling of Burning Emissions (FLAMBE) data indicated that its probable source was the Primorsky Krai Region of southeastern Russia. The decrease of $\tau_f(z, \infty)$ with decreasing altitude in Fig. 8b is thus consistent with viewing the decreasing values of the tail edge of the smoke plume as the plane passed underneath it. It is effectively a relevant example of what can go wrong when comparing in-situ data with columnar data (the case of an atmosphere whose state varies significantly during the sampling profile).

3.5. Comparisons with other profiling data sets

Dropsonde and AMALi profiles were acquired during Flight lines 4 and 10 while AMALi profiles were also acquired during Flight line 16 and 17 (detailed profiles of both types of data are given in Dethloff et al., 2009). The AMALi profiles show aerosol structure at altitudes of 1 km or greater for profiles acquired within 1½ hours and 4½ hours and a few hundred km of the Flight 4 and Flight 16 sunphotometer profiles (the ascending profiles showing analogous structure above 1 km altitude in Figs. 6 and 7). The AMALi profiles showed very low-altitude aerosol structure corresponding to the low turbidity event of Flight 10 (i.e. the profile of Fig. 4 which has no obvious aerosol structure and which was acquired quite close in time and space to the AMALi profile). The dropsonde data typically showed rather low inversion layer heights of a few hundred meters over the permanent ice pack region (Lampert et al., 2011, in review) where the sunphotometry profiles of Flights 4 and 10 were acquired (well below the aerosol structure seen in Fig. 6 for example). Only radiosonde data acquired at Inuvik was available for Flight 17 (the descending-profile smoke event of Fig. 8). This radiosonde data, acquired 7 h before (12Z) and 5 h after (24Z) the aircraft descent to Inuvik, was actually fairly invariant in terms of temperature and potential temperature changes across 12 h. There was no evident association to be made with the 6 km smoke plume aside from an apparent (optically insignificant) increase in relative humidity in the latter radiosonde profile between about 5 and 9 km.

4. Summary and conclusions

A series of Arctic sunphotometry flights were analyzed in terms of their multi-altitude, sub-micron (fine mode) information content. A spectral deconvolution algorithm (SDA) and a fine mode curvature algorithm (FMC) were applied to extract fine mode and coarse mode optical depth as well as the effective radius of the fine mode as a function of altitude. The fine mode optical depth was differentiated as a function of altitude to retrieve vertical profiles of fine mode extinction coefficient. These optical results were compared with volumetric altitude profiles of fine mode particle size distribution acquired by a UHSAS (Ultra High Sensitivity Aerosol Spectrometer).

There was a significant difference in amplitude between the computed extinction cross sections derived from equation (1c) and those derived from Mie calculations using log-normal means and standard deviations from the UHSAS; This means that either the difference $[\tau_f(0, \infty) - \tau_f(z_{max}, \infty)]$ is too large or the abundance $A_{N,f}(0, z_{max})$ is too small; its hard to imagine how the former quantity would be systematically in error by a factor ~ 5. In spite of this anomalous result, we found that $C_{f,emp.}$ was rather strongly correlated with $C_{f,Mie}$; such a correlation, resulting from the comparison of totally independent data seems rather extraordinary, however it would be disingenuous on our part to make anything of this result since we don't understand the large amplitude differences in the cross sections.

The extinction coefficients computed from the vertical derivatives of the fine mode optical depth showed some correlation with the UHSAS extinction coefficients as a function of altitude (either in an amplitude sense in the case of the low turbidity atmosphere (i.e. both profiles were weak in amplitude) to actual vertical correlation in the case of the chosen examples of substantial boundary layer turbidity). We showed a case where the division into fine and coarse mode optical depths significantly improved the quality of the derived extinction coefficients (i.e. as compared to a vertical derivative applied to the total AOD). The fine mode extinction coefficients are nonetheless extremely sensitive to subtle changes in fine mode optical depth slope with altitude and their validation is challenging at best.

The results for the retrieval of fine mode effective radius profiles indicated that, with the exception of one apparently anomalous case, the mean amplitudes (using the nominal value of the real part of the refractive index) were similar to within approximately 0.03 μm but that little could be determined in terms of being able to isolate a significant trend with altitude.

Finally, a relevant example was given of a high altitude smoke plume whose presence eliminated any hope of correlating the volumetric sampling information with the columnar optical information. This is simply a statement of the obvious; that the atmospheric state must be stable in order to make such comparisons.

Acknowledgments

The authors would like to thank four Canadian funding agencies, NSERC (National Sciences and Engineering Research Council), CFCAS (Canadian Foundation for Climate and Atmospheric Sciences), CFI (Canadian Foundation for Innovation) and FQRNT (Fonds de recherche sur la nature et les technologies, Québec) for their financial support. Valuable support was also provided by Environment Canada and NASA's AERONET project. Useful exchanges with Graeme Nott and Jeff Pierce of Dalhousie University were also very much appreciated.

Appendix. Optical relationships as a function of altitude

Columnar Relationships

The fine mode optical depth above the airplane is given by;

$$\begin{aligned}\tau_f(z, \infty) &= \int_z^{\infty}\int_0^{r_0} C(m,r,\lambda)n_f(r,z')d\log r dz' \\ &= \int_0^{r_0} C(m,r,\lambda)\frac{d\int_z^{\infty} N_f(z')dz'}{d\log r}d\log r \\ &= \int_0^{r_0} C(m,r,\lambda)\frac{dA_{N,f}(z,\infty)}{d\log r}d\log r \\ &\le C_f(m,\lambda,z,\infty) > A_{N,f}(z,\infty) \end{aligned} \quad (1a)$$

$$\text{where; } < C_f(m,\lambda,z,\infty) > \geq \frac{\int_0^{r_0} C(m,r,\lambda)\,\frac{dA_{N,f}(z,\infty)}{d\log r}\,d\log r}{\int_0^{r_0} \frac{dA_{N,f}(z,\infty)}{d\log r}\,d\log r}$$

$$= \frac{\int_0^{r_0} C(m,r,\lambda)\frac{dA_{N,f}(z,\infty)}{d\log r}\,d\log r}{A_{N,f}(z,\infty)}$$

The limit r_0 is the upper fine mode cutoff of the UHSAS, m is the complex refractive index, $C(m, r, \lambda)$ is the monodispersive extinction cross section, $dN_f(z)$ (the differential analog to what the UHSAS actually measures) is the number density across a logarithmic bin of width $d \log r$, $N_f(z)$ is the total number density integrated across all particle sizes and $A_N(z, \infty)$ is the vertically integrated abundance of the UHSAS number densities. If $<C_f(m, \lambda, z, \infty)>$ is approximately independent of z then equation (1) says that $\tau_f(z, \infty)$ is proportional to (z, ∞).

In actual fact we can only integrate the UHSAS number densities up to a maximum altitude of z_{max}. Accordingly;

$$\begin{aligned}\tau_f(z,\infty) &= \int_0^{r_0} C(m,r,\lambda)\frac{dA_{N,f}(z,z_{max})+A_{N,f}(z_{max},\infty)}{d\log r}d\log r\\ &\leq C_f(m,\lambda,z,z_{max})>A_{N,f}(z,z_{max})+\\ &< C_f(m,\lambda,z_{max},\infty)>A_{N,f}(z_{max},\infty)\\ &\leq C_f(m,\lambda,z,z_{max})>A_{N,f}(z,z_{max})+\tau_f(z_{max},\infty)\end{aligned} \quad (1b)$$

where $A_{N,f}(z, z_{max})$ can be computed from UHSAS number densities and $\tau_f(z_{max}, \infty)$ is the measured sunphotometer, fine mode optical depth at z_{max} (or more specifically the derived fine mode optical depth obtained from measured AOD spectra at z_{max}). One can then (a) use equation (1b) to estimate $\tau_f(z, \infty)$ given an estimate of $<C_f(m, \lambda, z, z_{max})>$ from Mie calculations or (b) estimate the average extinction cross section given sunphotometer estimates of $\tau_f(z, \infty)$ and $\tau_f(z_{max}, \infty)$ and a UHSAS estimate of $A_N(z, z_{max})$;

$$< C_f(m,\lambda,z,z_{max}) > \geq \frac{\tau_f(z,\infty)-\tau_f(z_{max},\infty)}{A_{N,f}(z,z_{max})} \quad (1c)$$

The effective radius of the fine mode ($r_{eff,f}$) can be computed directed from the UHSAS volumetric samples;

$$r_{eff,f}(z) = \frac{\int_0^{r_0} r^3\frac{dN_f}{d\log r}d\log r}{\int_0^{r_0} r^2\frac{dN_f}{d\log r}d\log r} \quad (2a)$$

However, the value of $r_{eff,f}$ computed from the SDA/FMC process is effectively an (above-aircraft) average quantity where the averaging kernel is column integrated number density;

$$r_{eff,f}(z,\infty) = \frac{\int_0^{r_0} r^3\frac{dA_{N,f}(z,\infty)}{d\log r}d\log r}{\int_0^{r_0} r^2\frac{dA_{N,f}\left(z,\infty\right)}{d\log r}d\log r} \quad (2b)$$

where $dA_{N,f}(z, \infty)$ is differential integrated number density across $d \log r$. Reversing the order of integration in equation (2) (proceeding in reverse fashion to the derivation of equation (1)) we have;

$$r_{eff,f}(z,\infty) = \frac{\int_0^{r_0} r^3\int_z^{\infty} n_f(r,z')dz'd\log r}{\int_0^{r_0} r^2\int_z^{\infty} n_f\left(r,z\right)dzd\log r} = \frac{\int_z^{\infty}\int_0^{r_0} r^3 n_f(r,z')d\log r\,dz'}{\int_z^{\infty}\int_0^{r_0} r^2 n_f\left(r,z\right)d\log r\,dz}$$

$$r_{eff,f}(z,\infty) = \frac{\frac{3}{4\pi}\int_z^{\infty} V_f(z')dz'}{\frac{1}{\pi}\int_z^{\infty} S_f(z')dz'} = \frac{3}{4}\frac{A_{V,f}\left(z,\infty\right)}{A_{S,f}\left(z,\infty\right)} \quad (3a)$$

where $V_f(z')$ and $S_f(z')$ are the volume and the projected surface of all particles in the size distribution at altitude z per unit volume of air. $A_{V,f}(z, \infty)$ and $A_{S,f}(z, \infty)$ are the columnar densities for the volume and surface (respectively, the volume of all particles per unit surface and the projected surface of all particles per unit ground surface). Integrating over r and then z' was the actual process that we applied to the UHSAS data. Finally, because we only integrate the UHSAS from z to z_{max}, equation (3a) must be modified. Partitioning the integrals into subintegrals above and below z_{max} yields (after a little algebra);

$$\begin{aligned}r_{eff,f}(z,\infty) &= (1-\gamma)r_{eff,f}(z,z_{max})+\gamma r_{eff,f}(z_{max},\infty) \text{ where } \gamma\\ &= \frac{A_{S,f}(z_{max},\infty)}{A_{S,f}\left(z,\infty\right)}, \text{and } 0\leq\gamma\leq 1\end{aligned} \quad (3b)$$

The partitioned effective radii, $r_{eff,f}(z, z_{max})$ and $r_{eff,f}(z_{max}, \infty)$ are given by equation (3a) with appropriate changes in the altitude limits. The effective radius $r_{eff,f}(z, z_{max})$ is then computed from the UHSAS data. The effective radii above z_{max} come from the sunphotometer data while (the typically small) γ parameter can be approximated by $\gamma \cong \tau_f(z_{max}, \infty)/\tau_f(z, \infty)$.

Volumetric relationships

The fine mode optical depth is given by the fundamental equation (c.f. the defining equation leading to equation (1a));

$$\tau_f\left(z,\infty\right) = \int_z^{\infty}\int_0^{r_0} C(m,r,\lambda)\,n_f(r,z')d\log r\,dz'$$

Integrating this over log r yields;

$$\tau_f\left(z,\infty\right) = \int_z^{\infty}\kappa_f(z')dz' = \int_z^{\infty} < C(m,\lambda,z')>N_f(z')dz'$$

where $\kappa_f(z')$ is the extinction coefficient and where the size distribution averaged extinction cross section is given by;

$$< C(m,\lambda,z') \geq \frac{\int_0^{r_0} C(m,r,\lambda)n_f(r,z')d\log r}{\int_0^{r_0} n_f(r,z')d\log r} = \frac{\int_0^{r_0} C(m,r,\lambda)n_f(r,z')d\log r}{N_f(z')}$$

A fine-mode extinction coefficient profile can thus be retrieved from a $\tau_f(z, \infty)$ profile by the application of derivatives across small altitude intervals;

$$\kappa_f(z') \leq C(m,\lambda,z') > N_f(z') = -\frac{d\tau_f(z,\infty)}{dz} \quad (4)$$

where a negative sign has been affixed to the optical depth derivative because we want the extinction coefficient to be defined as positive and because an increase in altitude will produce a decrease in any optical depth (or vice versa) in a fixed-state atmosphere. If the atmosphere deviates significantly from a fixed state atmosphere, then all bets are off and the extinction coefficient, defined as per equation (4), can be negative or positive.

References

Atkinson, D.B., Massoli, P., O'Neill, N.T., Quinn, P.K., Covert, D.S., Brooks, S.D., Lefer, B., 2010. Comparison of in situ and columnar spectral measurements during TexAQS-GoMACCS 2006: testing parameterizations for estimating aerosol fine mode optical properties. Atmospheric Chemistry and Physics 10, 51–61. doi:10.5194/acp-10-51-2010.

Dethloff, K., Herber, A., Maturilli, M., Neuber, R., Lampert, A., Brauner, R., Rinke, A., Mielke, M., 2009. Dropsondes and AMALI during PAM-ARCMIP, PAM-ARCMIP. Environment Canada, Toronto.

Dubovik, O., Smirnov, A., Holben, B.N., King, M.D., Kaufman, Y.J., Eck, T.F., Slutsker, I., 2000. Accuracy assessments of aerosol optical properties retrieved from AERONET sun and sky-radiance measurements. Journal of Geophysical Research 105, 9791–9806.

Hoffman, A., Ritter, C., Stock, M., Shiobara, M., Lampert, A., Maturilli, M., Orgis, T., Neuber, R., Herber, A., 2009. Ground-based lidar measurements from Ny-Alesund during ASTAR 2007. Atmospheric Chemistry and Physics 9, 9059–9081.

Lampert, A., Maturilli, M., Ritter, C., Hoffmann, A., Stock, M., Herber, A., Birnbaum, G, Neuber, R., Dethloff, K., Orgis, T., Stone, R.S., Brauner, R., Kässbohrer, J., Haas, C., Makshtas, A., Sokolov, V., Liu P. Dropsonde and lidar characterization of the boundary layer over Arctic sea ice during PAMARCMiP, Atmospheric Environment, in review

Nott, G.J., Duck, T.J., Doyle, J.G., Coffin, M.E.W., Perro, C., Thackray, C.P., Drummond, J.R., Fogal, P.F., McCullough, E., Sica, J.R. A remotely-operated lidar for aerosol, temperature, and water vapor profiling in the High Arctic, Journal of Atmospheric and Oceanic Technology, in press.

O'Neill, N.T., Eck, T.F., Smirnov, A., Holben, B.N., Thulasiraman, S., 2003. Spectral discrimination of coarse and fine mode optical depth. Journal of Geophysical Research 108, 4559. doi:10.1029/2002jd002975.

O'Neill, N.T., Thulasiraman, S., Eck, T.F., Reid, J.S., 2005. Robust optical features of fine mode size distributions: application to the Québec smoke event of 2002. Journal of Geophysical Research 110, D11207. doi:10.1029/2004JD005157.

O'Neill, N.T., Thulasiraman, S., Eck, T.F., Reid, J.S., 2008a. Correction to the effective radius expression in O'Neill et al. (2005). Journal of Geophysical Research 113, D24203. doi:10.1029/2008JD011334.

O'Neill, N.T., Pancrati, O., Baibakov, K., Eloranta, E., Batchelor, R.L., Freemantle, J., McArthur, L.J.B., Strong, K., Lindenmaier, R., 2008b. Occurrence of weak, submicron, tropospheric aerosol events at high Arctic latitudes. Geophysical Research Letters 35, L14814. doi:10.1029/2008GL033733.

Saha, A., O'Neill, N.T., Eloranta, E., Stone, R.S., Eck, T.F., Zidane, S., Daou, D., Lupu, A., Lesins, G., Shiobara, M., McArthur, L.J.B., 2010. Pan-Arctic sunphotometry during the ARCTAS-A campaign of April 2008. Geophysical Research Letters 37, L05803. doi:10.1029/2009GL041375.

Shinozuka, Y., Redemann, J., Livingston, J.M., Russell, P.B., Clarke, A.D., Howell, S.G., Freitag, S., O'Neill, N.T., Reid, E.A., Johnson, R., Ramachandran, S., McNaughton, C.S., Kapustin, V.N., Brekhovskikh, V., Holben, B.N., McArthur, L.J.B., 2011. Airborne observation of aerosol optical depth during ARCTAS: vertical profiles, inter-comparison and fine-mode fraction. Atmospheric Chemistry and Physics 11, 3673–3688. doi:10.5194/acp-11-3673-2011.

Stachlewska, I.S., Neuber, R., Lampert, A., Ritter, C., Wehrle, G., 2010. AMALi – the airborne Mobile aerosol lidar for Arctic research. Atmospheric Chemistry and Physics 10, 2947–2963. doi:10.5194/acp-10-2947-2010.

Stone, R.S., Herber, A., Vitale, V., Mazzola, M., Lupi, A., Schnell, R.C., Dutton, E.G., Maturilli, M., 2010. A three dimensional characterization of Arctic aerosols from airborne Sun photometer observations: PAMARCMIP, April 2009. Journal of Geophysical Research 115, D13203. doi:10.1029/2009JD013605.

Toledano, C., Wiegner, M., Groß, S., Fredenthaler, V., Gasteiger, J., Müller, D., Müller, T., Schladitz, A., Weinzierl, B., Torres, B., O'Neill, N.T., 2011. Optical properties of aerosol mixtures derived from sun-sky radiometry during SAMUM-2. Tellus 63B, 635-648, doi:10.1111/j.1600-0889.2011.00573.x.

Tomasi, C., Vitale, V., Lupi, A., Di Carmine, C., Campanelli, M., Herber, A., Treffeisen, R., Stone, R.S., Andrews, E., Sharma, S., Radionov, V., von Hoyningen-Huene, W., Stebel, K., Hansen, G.H., Myhre, C.L., Wehrli, C., Aaltonen, V., Lihavainen, H., Virkkula, A., Hillamo, R., Strom, J., Toledano, C., Cachorro, V.E., Ortiz, P., de Frutos, A.M., Blindheim, S., Frioud, M., Gausa, M., Zielinski, T., Petelski, T., Yamanouchi, T., 2007. Aerosols in polar regions: a historical overview based on optical depth and in situ observations. Journal of Geophysical Research 112, D16205. doi:10.1029/2007JD008432.

Treffeisen, R.E., Thomason, L.W., Strom, J., Herber, A.B., Burton, S.P., Yamanouchi, T., 2006. Stratospheric Aerosol and Gas Experiment (SAGE) II and III aerosol extinction measurements in the Arctic middle and upper troposphere. Journal of Geophysical Research 111, D17203,. doi:10.1029/2005JD006271.

Glossary

A_N (z_1, z_2): Integrated number density or abundance between altititudes z_1 and z_2 (cm^{-2})
AOD: Aerosol Optical Depth (used interchangeably with τ_a (although the latter is usually employed when referring to the 500 nm SDA retrievals)
C: Extinction cross section (cm^2)
FMC: Algorithm for the extraction of $r_{eff,f}$ from SDA outputs of α_f and α_f'
∞*:* Optical infinity.
$\kappa_f(z)$: Fine mode extinction coefficient at 500 nm wavelength (km^{-1})
$N(z)$, $N_f(z)$: Number density at altitude z (cm^{-3})
SDA: Spectral Deconvolution Algorithm for extracting τ_a, τ_f and τ_c at 500 nm from measured AOD spectra ($\tau_a(\lambda)$)
$r_{eff,f}$: Effective radius of the fine mode (μm)
τ_f: short form for $\tau_f(0, \infty)$
$\tau_f(z_1, z_2)$: Fine mode optical depth at 500 nm wavelength between altititudes z_1 and z_2
τ_c: short form for $\tau_c(0, \infty)$
$\tau_c(z_1, z_2)$: Coarse mode optical depth at 500 nm wavelength between altititudes z_1 and z_2
τ_a: short form for $\tau_a(0, \infty)$
$\tau_a(z_1, z_2)$: Total aerosol optical depth at 500 nm wavelength between altititudes z_1 and z_2
UHSAS: Ultra High Sensitivity Aerosol Spectrometer
z: Altitude above sea-level (km). Generally this refers to the airplane altitude
z_{max}: Maximum altitude of a given profile (km)